RSC Advances

PAPER

View Article Online
View Journal | View Issue



Cite this: *RSC Adv.*, 2025, **15**, 36414

# Electrochemical evaluation of EVA/ZnO nanocomposite coatings: achieving superior electrochemical corrosion protection in harsh environments

Mohamed M. Abdel-Aal,[a] Mohamed Sh. Abdel-wahab, *[a] E. M. Elsayed,[b] S. I. El-Dek [a] and M. R. Hussein[a]

The development of polymer-based composite coatings with high quality and efficiency for corrosion resistance has become increasingly significant, particularly in harsh environmental conditions. In this context, a composite coating (EMZ3) was successfully formulated with an optimal blending ratio of ethylene-vinyl acetate (EVA) copolymer and 60% synthesized nano-sized zinc oxide (ZnO), tailored *via* co-precipitation to ensure uniform dispersion and enhanced corrosion resistance, using the mechanical blending technique. This environmentally friendly coating demonstrated exceptional protective performance compared to other coatings with varying ZnO concentrations. The mechanical blending method enhanced the coating's long-term protective capabilities through homogeneous and proportional distribution of the components. Electrochemical impedance spectroscopy (EIS) results indicated increasing charge transfer resistance and sustained stability over a 28 day immersion period in a 3.5% sodium chloride solution. The creation of environmentally friendly, corrosion-resistant coatings is made possible by this research's innovative integration of recycled EVA/ZnO composites from industrial waste. This study opens avenues for incorporating recycled polymers from industrial waste, enabling the production of more efficient protective coatings and environmentally friendly solutions.

Received 28th July 2025
Accepted 23rd September 2025

DOI: 10.1039/d5ra05455a

rsc.li/rsc-advances



## 1. Introduction

Metal corrosion is one of the most significant challenges affecting the economic viability of nations. This is similar to a malignancy within a metal, leading to its electrochemical deterioration.[1,2] Global losses attributed to corrosion and its mitigation efforts are estimated at approximately $2.8 trillion annually, equivalent to approximately 3.4% of the world's gross domestic product. Corrosion affects critical sectors, such as infrastructure, transportation, and energy, contributing to production halts, structural failures, and catastrophic safety risks.[2–8] For instance, the 2013 Lac-Mégantic railway disaster, in which rust on oil tankers caused leaks and devastating explosions, exemplifies such risks.[9,10] The catastrophic consequences of corrosion are particularly evident in developing and impoverished nations, where inadequate maintenance owing to resource scarcity often results in losses approaching 5% of their gross domestic product.[11]

Mild steel, which is widely utilized in industries such as pipelines, construction, and automotive applications owing to its mechanical strength, formability, enhanced properties, and low cost, is particularly susceptible to corrosion, necessitating early protective strategies.[12–14] Previous research has established that corrosion is a significant challenge that cannot be eradicated but can be mitigated. Various techniques and mechanisms have been employed, including advanced coatings and effective corrosion inhibitors, spurring research on permanent and cost-effective solutions.[15–17] Protective coatings against corrosion are diverse, encompassing metallic, organic, and inorganic types, each with distinct strengths and limitations. For example, ceramic coatings such as alumina and zirconia are chemically inert and resistant to corrosion at high temperatures, but they are brittle and entail high manufacturing costs.[18–21] Enamel coatings, derived from glass, offer homogeneity and impermeability but are fragile under mechanical stress. Composite materials, which combine polymers and fibers, enhance strength and corrosion resistance but face challenges related to sustainability and manufacturing complexity.[22,23]

Polymeric coatings have gained prominence owing to their flexibility, adhesion strength, and ability to shield metals from moisture, salts, and oxygen. Examples include epoxy,

[a]*Materials Science and Nanotechnology Department, Faculty of Postgraduate Studies for Advanced Sciences, Beni-Suef University, Beni-Suef 62511, Egypt. E-mail: mshaabancnt@psas.bsu.edu.eg*

[b]*Central Metallurgical Research and Development Institute (CMRDI), Helwan, P. O. Box 87, Cairo 11421, Egypt*

polyurethane, and vinyl coating. However, their protection against ultraviolet radiation is short-lived, and defects such as micropores and fine cracks formed during curing create pathways for corrosive agents to enter the substrate.[24–26] Ethylene-vinyl acetate (EVA), a copolymer of ethylene and vinyl acetate, exhibits performance variations based on its vinyl acetate (VA) content, typically ranging from 10–40%. At 22% VA content, EVA achieves an optimal balance of flexibility, adhesion, and chemical resistance, making it ideal for forming homogeneous and durable coatings. It is a polymer that is similar in suppleness and flexibility to elastomeric materials, but it can be processed in the same way as other thermoplastics. The material possesses barrier properties, low-temperature toughness, stress-crack resistance, hot-melt adhesive waterproof properties, and resistance to UV radiation, in addition to excellent clarity and gloss.[27,28]

With advancements in corrosion-resistant coatings, the integration of self-healing mechanisms within ethylene vinyl acetate (EVA) composites incorporating zinc oxide (ZnO) has emerged as a promising strategy for enhancing durability.[29,30] Recent advancements in self-healing technologies, which utilize encapsulated healing agents activated by damage, can significantly prolong the lifespan of coatings in extreme environments. EVA can form films and work with nanomaterials; therefore, ZnO nanoparticles added to improve UV resistance, hydrophobicity, and electrochemical protection. ZnO is a non-toxic and cost-effective semiconductor that reduces coating porosity and provides sacrificial protection through electrochemical activity.[31,32] Methods for incorporating ZnO into EVA, such as *in situ* polymerization, mechanical blending, and solvent-assisted dispersion (also known as solution blending), have been reported, with solution blending noted for its superior uniform nanoparticle distribution, significantly enhancing coating performance.[33–35] This process involves dissolving EVA in solvents such as toluene and adding ZnO under controlled heating (60–80 °C), minimizing agglomeration, and ensuring coating homogeneity compared to the inconsistent results of mechanical blending or the control complexities of *in situ* polymerization.[36–39]

These advancements herald a new era of high-performance coatings tailored to meet industrial requirements. Exploring EVA coatings infused with ZnO nanoparticles not only underscores progress in corrosion protection but also invites a broader examination of alternative materials and methods that could complement or enhance these coatings.[40–44]

Building on this, the study paves the way for developing an EVA-based coating with 22% vinyl acetate (VA) content, reinforced with ZnO nanoparticles (40–80 wt%), to protect mild steel from corrosion. The coating was prepared using a solution blending technique, with this innovative approach aiming to address gaps and contribute to the field of corrosion protection. The efficacy of the coating was rigorously evaluated using electrochemical impedance spectroscopy (EIS) techniques in a 3.5% NaCl solution. This method is used to investigate the corrosion dynamics, barrier properties, and long-term stability. The scarcity of literature highlighting the use of EVA-based coatings integrated with nanomaterials for corrosion protection was the primary motivation for this research. This study aims to deliver a widely applicable, environmentally friendly coating that redefines corrosion protection for mild steel, pushing the boundaries of materials science toward practical and industry-ready solutions.

## 2. Experimental

### 2.1. Materials

In this study, ethylene-vinyl acetate copolymer (EVA), characterized by the chemical formula $(C_2H_4)_n(C_4H_6O_2)_m$, a molecular weight of approximately 342.43 g mol$^{-1}$, and a density of about 0.95 g cm$^{-3}$, was used as the polymer matrix. The EVA, sourced as transparent granules (Grade 3522, Saudi) with a vinyl acetate content of 22 wt% and a granule thickness of 2–3 mm, was employed for the preparation of the composites. Zinc nitrate hexahydrate ($Zn(NO_3)_2\cdot 6H_2O$, purity: 98%), sodium hydroxide (NaOH, purity: ≥97%), citric acid ($C_6H_8O_7$, purity: 99.5%), toluene (purity: ≥99.9%), acetone (purity: ≥99.5%), and ethanol (purity: 99.8%) were procured from Sigma-Aldrich (St. Louis, MO, USA). Mild steel substrates (composition: Fe (99.73%)–C (0.06%)–Mn (0.10%), dimensions: 1.5 × 1.5 cm, thickness: 1 mm) were supplied by EZZ Steel Company (Suez, Egypt). All chemicals and materials were utilized as received without further purification to ensure consistency with industrial application protocols and reproducibility of experimental conditions.

### 2.2. Substrate preparation

Mild steel coupons (1.5 × 1.5 cm, thickness: 1 mm) were cut using a precision shear cutter. The substrates were mechanically polished sequentially with SiC abrasive papers (grades 400, 800, and 1200) to achieve uniform surface roughness. To remove residual grease and contaminants, the samples were ultrasonically cleaned in acetone for 10 min, followed by ethanol and bi-distilled water. The sonication process (Elmasonic S 60 H, 50 kHz, 550 W) was employed to ensure thorough removal of embedded particles. After cleaning, the substrates were dried in an oven at 60 °C for 1 h.

### 2.3. Synthesis of ZnO nanoparticles

Zinc oxide nanoparticles (ZnO NPs) were synthesized *via* a co-precipitation method. Zinc nitrate hexahydrate ($Zn(NO_3)_2\cdot 6H_2O$, 5.94 g, 20 mmol) was dissolved in 100 ml distilled water under magnetic stirring (500 rpm). Separately, sodium hydroxide (NaOH, 3.2 g, 80 mmol) and citric acid ($C_6H_8O_7$, 2 g, 10.4 mmol) were dissolved in 50 ml of distilled water. Citric acid was added before NaOH to chelate $Zn^{2+}$ ions, controlling particle growth and enhancing colloidal stability as a stabilizing agent and preventing agglomeration. The NaOH solution was added dropwise (1 ml min$^{-1}$) into the zinc nitrate solution. The pH of the mixture was adjusted to 10 using a pH meter (Metrohm Instruments 826, 6 V DC, 15 mA), inducing the formation of $Zn(OH)_2$ precipitate. The solution was maintained at 65 °C with continuous stirring for 60 min. The precipitate was centrifuged (5000 rpm, 10 min), washed 5–6 times with bi-

distilled water and ethanol to remove unreacted ions, and dried at 80 °C for 10 h. Finally, the powder was annealed in a muffle furnace to ensure crystallinity and remove residual hydroxyl groups, critical for ZnO's anti-corrosive properties (Nabertherm L5/11) at 500 °C for 3 h to convert $Zn(OH)_2$ to ZnO (confirmed by XRD analysis).

### 2.4. Coating formulation and deposition

Four coating formulations were prepared: EMZ1, consisting of 5 g polymer matrix (EVA (ethylene vinyl acetate)) dissolved in 45 g toluene, and EMZ1–EMZ4, comprising the same polymer matrix with sample 1; pure EVA, samples 2–4; EVA with increasing ZnO wt% nanoparticles content 80%, 60% and 40% respectively. The mixtures were homogenized *via* magnetic stirring (800 rpm, 30 min) at 80 °C to ensure uniform dispersion of ZnO NPs. The coatings were applied to the mild steel substrates using a drop-casting technique. To achieve consistent thickness (~50 μm), the solution was deposited at a rate of 0.1 ml $cm^{-2}$, followed by leveling with a spin coater (Laurell WS-650Mz) at 1000 rpm for 30 s which optimized to avoid cracking and ensure homogeneous thickness The coated samples were cured at 120 °C for 2 h. Fig. 1 provides a concise depiction of the synthesis of the EVA/ZnO composite coating on mild steel.

### 2.5. Characterization and testing

X-ray diffraction (XRD) was performed using a PANalytical Empyrean (Netherlands) and a Bruker Axis D8 diffractometer with Cu-K$\alpha$ radiation ($\lambda$ = 1.5406 Å), a secondary monochromator, a 2$\theta$ range of 20° to 80°, and a scan rate of 2° $min^{-1}$ to characterize the crystalline structure, phase composition, and dispersion of ZnO nanoparticles within the polymer matrix across all samples (EMZ1–EMZ4). Additionally, coating uniformity and ZnO dispersion were analyzed using scanning electron microscopy (SEM, JEOL JSM-IT800) coupled with energy-dispersive X-ray spectroscopy (EDS) to analyze coating morphology and map elemental distribution (*e.g.*, Zn, C, O) to verify homogeneity. Meanwhile, we conducted thermogravimetric analysis (TGA) using the thermal gravimetric analyzer, SENSYS evo TG-DSC, to assess thermal stability by heating samples from 25 °C to 800 °C under nitrogen. Besides, Fourier-transform infrared spectroscopy (FTIR; Bruker, Germany) was used to elucidate chemical compatibility between ZnO and the polymer, ensuring no adverse interactions compromising coating stability, functional groups, and interfacial interactions between the polymer matrix and ZnO nanoparticles across all samples (EMZ1–EMZ4). Also, the thicknesses of the prepared nanocomposite coatings were measured with a surface profiler (DektakXT, Bruker, Germany). Finally, X-ray photoelectron spectroscopy was collected on K-ALPHA (Thermo Fisher Scientific, USA) with monochromatic X-ray Al K-alpha radiation −10 to 1350 eV spot size 400 micrometer at pressure $10^{-9}$ mbar with full spectrum pass energy 200 eV and at narrow spectrum 50 eV, and was employed on the optimal coating (EMZ2 and EMZ3, selected post-corrosion testing) to confirm surface composition and ZnO passivation mechanisms after immersion in 3.5% NaCl.

All electrochemical measurements were assessed in 3.5 wt% NaCl solution (were procured from Sigma-Aldrich) at room temperature was performed with a three-electrode system, in which a platinum mesh (of area 1.25 $cm^2$), a saturated Ag/AgCl electrode (HANA company, Italy), and the coated mild steel with area of 1.25 $cm^2$ were used as counter electrode, reference electrode, and working electrode, respectively. Electrochemical impedance spectroscopy (EIS) curve analysis, impedance spectra (frequency range: 100 kHz to 10 mHz, amplitude: 10 mV) were modeled using ZSimpWin software to extract charge-transfer resistance ($R_{ct}$) and coating capacitance ($C_c$), reflecting barrier properties against electrolyte penetration. All performed in 3.5 wt% NaCl solution using a potentiostat (AUTOLAB

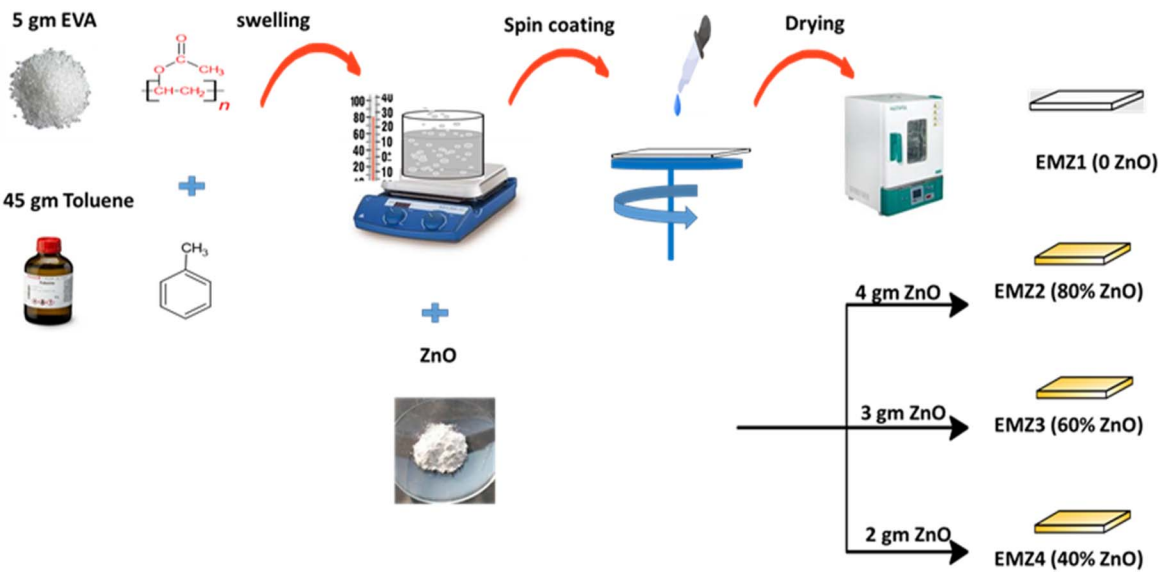


Fig. 1 The schematic representation for the synthesis of EVA/ZnO composite coating.

PGSTAT 302N, Metrohm, Switzerland, Ag/AgCl reference electrode), to evaluate the corrosion resistance and coating efficiency of the samples (EMZ1–EMZ4).

## 3. Results and discussion

### 3.1. Characterization of EVA copolymer/ZnO

The FTIR spectra were elucidated in Fig. 2a, which reflected the interplay between ZnO nanoparticles and the EVA polymer matrix. The prepared samples with varying ZnO nanoparticle ratios were depicted in Fig. 2a, confirming successful incorporation across samples EMZ2–EMZ4. ZnO's signature Zn–O stretching modes at 473 $cm^{-1}$ and 721 $cm^{-1}$ intensify from EMZ2 to EMZ4, mirroring the rising ZnO content and signaling robust embedding within the polymer. EVA's characteristic $CH_2$ rocking mode at 700–750 $cm^{-1}$ strengthens with increasing ZnO, a testament to enhanced crystallinity driven by ZnO's integration, underscoring effective dispersion.[45] A subtle band at 1033 $cm^{-1}$, likely EVA's C–O stretch overlapping with ZnO surface groups, grows with ZnO content, hinting at hydrogen bonding between ZnO's hydroxyls and EVA's polar groups.[46] Key EVA bands at 1738 $cm^{-1}$ (C=O stretching vibration), 1238 and 1020 $cm^{-1}$ (C–O stretching vibration) attributed to the asymmetric C–O–C stretching observed in both spectra serves as evidence for the existence of cross-linked segments within the polymer structure, 1465 $cm^{-1}$ ($CH_2$ bending vibration), and 1370 $cm^{-1}$ ($CH_3$ bending vibration) remain consistent. However, the C=O band may shift or broaden in EMZ2–EMZ4 due to ZnO interactions, enhancing composite compatibility.[47,48] A notable band at 1400 $cm^{-1}$ across all samples, likely a shifted $CH_3$ bending mode from 1370 $cm^{-1}$, reflects toluene salvation or thermal processing effects at 80 °C, rooted in EVA's matrix.[49] Intriguingly, a 1940 $cm^{-1}$ band emerges in EMZ2 and EMZ3, possibly an overtone of EVA's C=O or C–O modes amplified by ZnO interactions, though absent in EMZ1 (pure EVA) and EMZ4, suggesting a concentration-dependent effect or scattering artifact.[50] A 3026 $cm^{-1}$ band in EMZ2 points to residual toluene or ZnO scattering, while a broad 3400–3500 $cm^{-1}$ band indicates ZnO surface hydroxyls, diminished by heating.[51] These spectral insights compellingly affirm the successful synthesis of EVA/ZnO nanocomposites, inviting further exploration of their enhanced properties.

Also, Fig. 2b displays the XRD of EVA co-polymer coating designed to protect mild steel from corrosion, with a focus on the structural modifications induced by incorporating zinc oxide (ZnO) nanoparticles at varying concentrations. The XRD pattern of the pristine EVA copolymer coating exhibited characteristic broad peaks at $2\theta$ values of approximately 21.28° (110) and 23.44° (200), consistent with the semi-crystalline or amorphous nature reported in prior studies for this polymer.[52] These broad peaks arise from the disordered molecular arrangement and inherent chain flexibility of the polymer, which enhance the coating's uniformity, processability, and adhesion to the mild steel substrate. The incorporation of ZnO nanoparticles into the EVA co-polymer matrix at concentrations of 40%, 60%, and 80% by weight profoundly altered the X-ray diffraction (XRD) patterns, revealing distinct ZnO and polymer diffraction features. The prepared ZnO nanoparticles exhibited sharp, intense peaks at $2\theta$ values of 31.8°, 34.4°, 36.3°, 47.5°, 56.6°, 62.8°, 66.4°, 67.9°, 69.1°, 72.5°, 76.9°, and 77.2°, corresponding to the (100), (002), (101), (102), (110), (103), (200), (112), (201), (004), (202), and (104) planes of the hexagonal Wurtzite structure, as confirmed by JCPDS card no. 36-1451. The nanoscale nature of the ZnO particles was verified using the Scherrer equation,

$$D = \frac{K\lambda}{\beta \cos \theta} \quad (1)$$

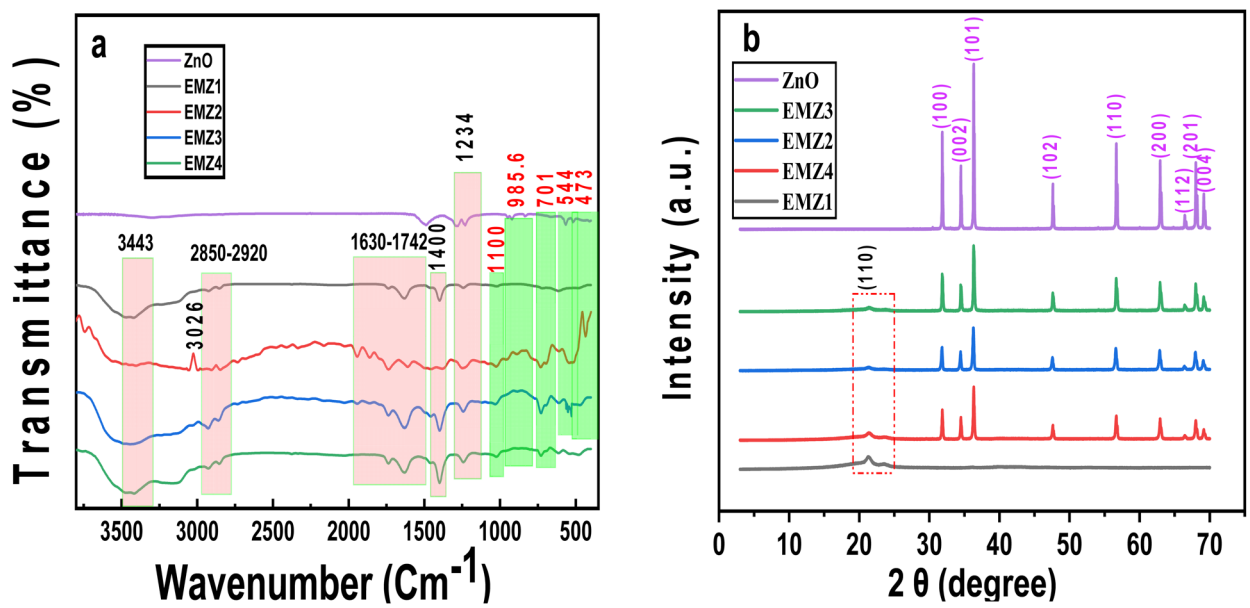


Fig. 2 (a) FT-IR spectra of EMZ1, EMZ2, EMZ3, and EMZ4. (b) XRD patterns of ZnO, EMZ1, EMZ2, EMZ3, and EMZ4.

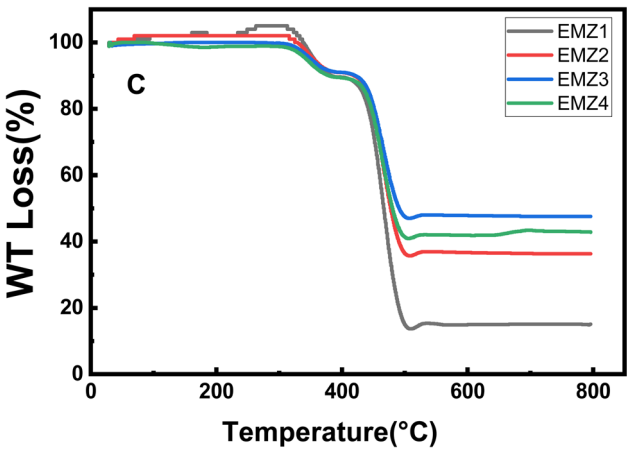


Fig. 3 TGA curves of EMZ1, EMZ2, EMZ3, and EMZ4.

where $D$ is the crystallite size, $K$ is the shape factor (~0.9), $\lambda$ is the X-ray wavelength (1.5406 Å for Cu Kα), $\beta$ is the full width at half maximum (FWHM) in radians, and $\theta$ is the Bragg angle.[53]

For the ZnO peaks at the previous $2\theta$ values, the average crystallite size is 72.8 nm, indicating a high surface area that enhances interfacial interactions with the EVA matrix. However, ZnO peak intensities decreased with increasing nanoparticle content, likely due to agglomeration or enhanced X-ray absorption by the polymer at higher loadings. Concurrently, the EVA peaks at 21.28° (110) and 23.44° (200) exhibited reduced intensity and increased broadening with higher ZnO content, reflecting diminished crystallinity and lattice strain induced by nanoparticle incorporation, as supported by Wang *et al.*, 2007. Composite coatings with ZnO loadings of 40%, 60%, and 80% by weight exhibited both ZnO and polymer diffraction features. Quantitative analysis of the XRD patterns showed a relative intensity ratio ($Intensity_{polymer}/Intensity_{ZnO}$) of [0.73, 0.70, 0.47 for 40%, 60%, 80% ZnO] for the polymer's characteristic peak at $2\theta = [21.2°]$ and the ZnO (101) peak at $2\theta = 36.3°$. This decreasing ratio with increasing ZnO content indicates a progressive disruption of the polymer's crystalline order, enhancing the coating's density and reducing porosity, thereby improving its barrier properties against corrosive agents like water and chloride ions. The reduction in polymer peak intensity suggests that ZnO nanoparticles disrupt the polymer's crystalline domains, likely due to lattice strain or steric effects, which may improve the coating's toughness and adhesion to the substrate.

### 3.2. Thermal degradation study of EVA–ZnO composites *via* TGA

As depicted in Fig. 3, thermogravimetric analysis (TGA) of four polymer coating samples, each incorporating different nanomaterial concentrations to improve corrosion resistance on mild steel substrates, highlights a compelling correlation between nanomaterial content and thermal stability. The mass loss profile of ethylene-vinyl acetate (EVA), shown in Fig. 3, exhibits a two-stage thermal degradation process. The first stage involves deacetylation, where acetate side groups are eliminated, leading to the formation of an unsaturated polymer backbone at range of temperatures (300–400 °C), known as polyene.[54]

The subsequent stage is characterized by allylic chain scission of the polyene, leading to complete thermal degradation at elevated temperatures,[55] as illustrated in eqn (2) and (3).

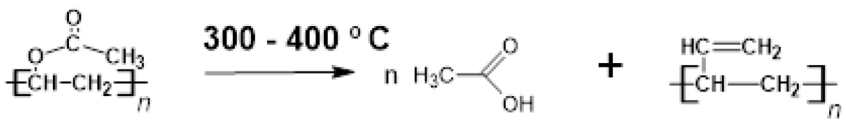


(2)

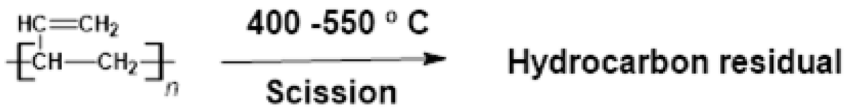


(3)

The incorporation of tungsten into the EVA matrix significantly enhances its thermal stability, as evidenced by the TGA profiles. The composites exhibit a shift toward higher degradation temperatures with increasing zinc oxide content. Specifically, the baseline sample (EMZ1), which is devoid of nanomaterials, undergoes a two-step decomposition, losing 15.45% of its mass between 273.12 °C and 398.64 °C, followed by a substantial 74.2% loss from 412.4 °C to 522.4 °C, resulting in a mere 14.7% residual mass (3.2 mg). In contrast, samples incorporating nanomaterials exhibit a delayed onset of decomposition, whereas the introduction of zinc oxide reduces this loss substantially. As detailed in Table 1, sample EMZ2, which contains the highest concentration of nanomaterials, extends the initial degradation step to 418.5 °C, resulting in approximately 12.2% mass loss. However, it retains only 36% of its residual mass (8.6 mg) after the second degradation step (422.8–516.6 °C). This is attributed to nanoparticle agglomeration, which disrupts homogeneous dispersion and compromises thermal protection. Similarly, EMZ3, with medium

Table 1 Thermal degradation characteristics of EVA composites

| Sample | Mass fraction of total weight loss (%) at (400–550 °C) | Residue% at (400–550 °C) |
|---|---|---|
| **EVA–ZnO composites samples** | | |
| EMZ1 | 74.3 | 14.7 |
| EMZ2 | 53.5 | 36.1 |
| EMZ3 | 25.3 | 66.8 |
| EMZ4 | 12.86 | 86.2 |

nanomaterial content, shows a first step degradation up to 420.5 °C with approximately 6.3% mass loss and retains 66.8% residual mass (13 mg) post-decomposition (422.6–520 °C). Most strikingly, EMZ4, which has the lowest nanomaterial loading, demonstrates exceptional stability, losing only about 1.15% mass between 86.5 °C and 240.9 °C, likely due to volatile evaporation rather than polymer breakdown, and retaining an impressive 86.2% residual mass (15.8 mg) after the second step (291.2–433.1 °C). This exceptional stability suggests that minimal nanomaterial incorporation optimizes cross-linking or char formation, acting as a thermal barrier. The findings elucidate the complex interactions among nanomaterial concentration, dispersion, and thermal properties, thereby providing a persuasive rationale for the optimization of low-concentration formulations aimed at developing cost-effective and high-performance anti-corrosion coatings.

### 3.3. SEM-EDX characterization of EVA co-polymer ZnO anti-corrosion coatings

A morphological study of the coatings was conducted using scanning electron microscope (SEM) images, captured before and after immersion in a 3.5% sodium chloride solution for 28 days. The SEM images, recorded at a 5-micron scale, revealed variations in the surface morphology of the coatings, dependent on the proportion of zinc oxide (ZnO) filler within the ethylene-vinyl acetate (EVA) copolymer matrix, with distinct coverage across the exposed surfaces. The images indicated homogeneity of micelles on the surface. It is evident from the images that samples EMZ2 and EMZ3, as depicted in Fig. 4b and c before immersion and (Fig. 4f and g) after immersion, respectively, displayed surface homogeneity prior to immersion, with greater uniformity and clarity observed in sample EMZ3 (Fig. 4c). After immersion, sample EMZ3 (Fig. 4g) exhibited reduced degradation of zinc ions into zinc chloride and zinc hydroxide, appearing as faint white patches with lower intensity compared to sample EMZ2 (Fig. 4f). This suggests that the ZnO proportion in sample EMZ3 was inferred to be well distributed and appropriately balanced within the polymer matrix, based on the observed surface homogeneity, minimizing aggregate formation that could otherwise compromise coating quality by creating accessible pathways within the polymer matrix, potentially exposing the metal to corrosion. Similarly, samples EMZ1 and EMZ4, as shown in Fig. 4a and d before immersion and (Fig. 4e and h) after immersion, exhibited coating deterioration and reduced quality, evidenced by the appearance of cracks and defects on the surface, as well as irregular aggregates

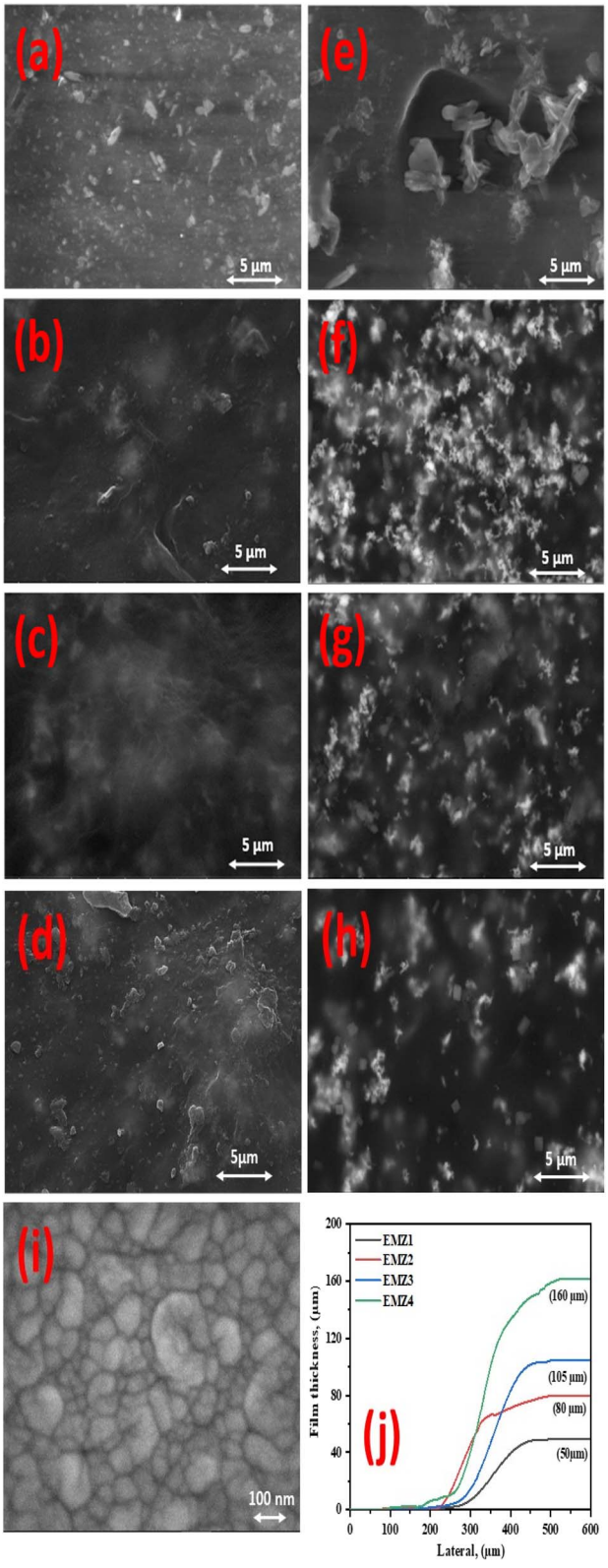


Fig. 4 SEM images of the (a and e) EMZ1; (b and f) EMZ2; (c and g) EMZ3; (d and h) EMZ4 coating surface, (i) ZnO nano particles and (j) the thickness of the prepared nano composite illustrating morphological changes under different exposure conditions.

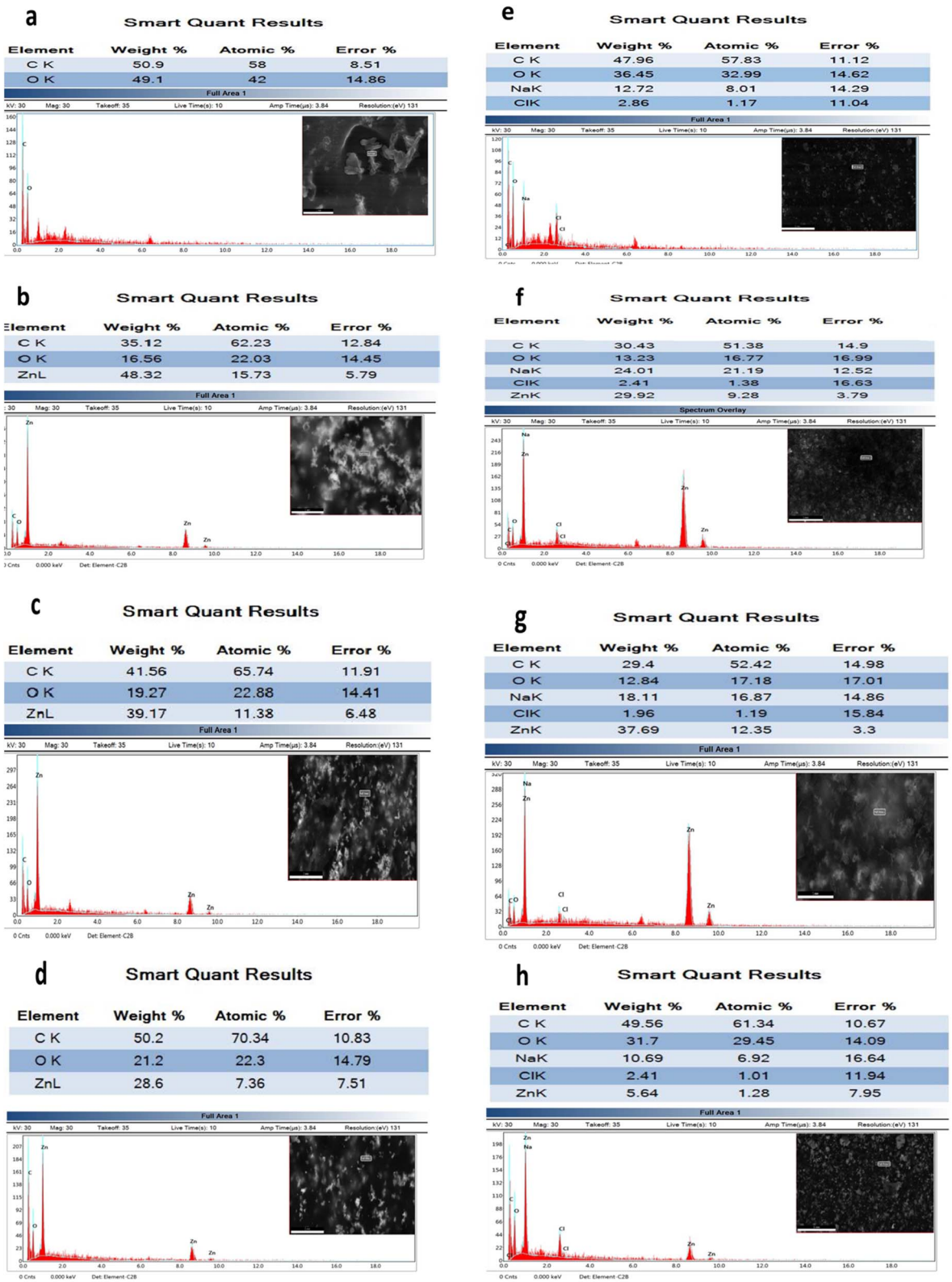


Fig. 5 EDS results of (a and e) EMZ1; (b and f) EMZ2; (c and g) EMZ3; (d and h) EMZ4 coatings.

within the polymer matrix, which became more pronounced after immersion. These aggregates form direct pathways to the metal surface. As we can notice from Fig. 4i, which represents the SEM image of the prepared ZnO nanoparticles. The particle size varies from 80–100 nm, which is aligned with the XRD result. The thickness profile curve, as depicted in Fig. 4j,

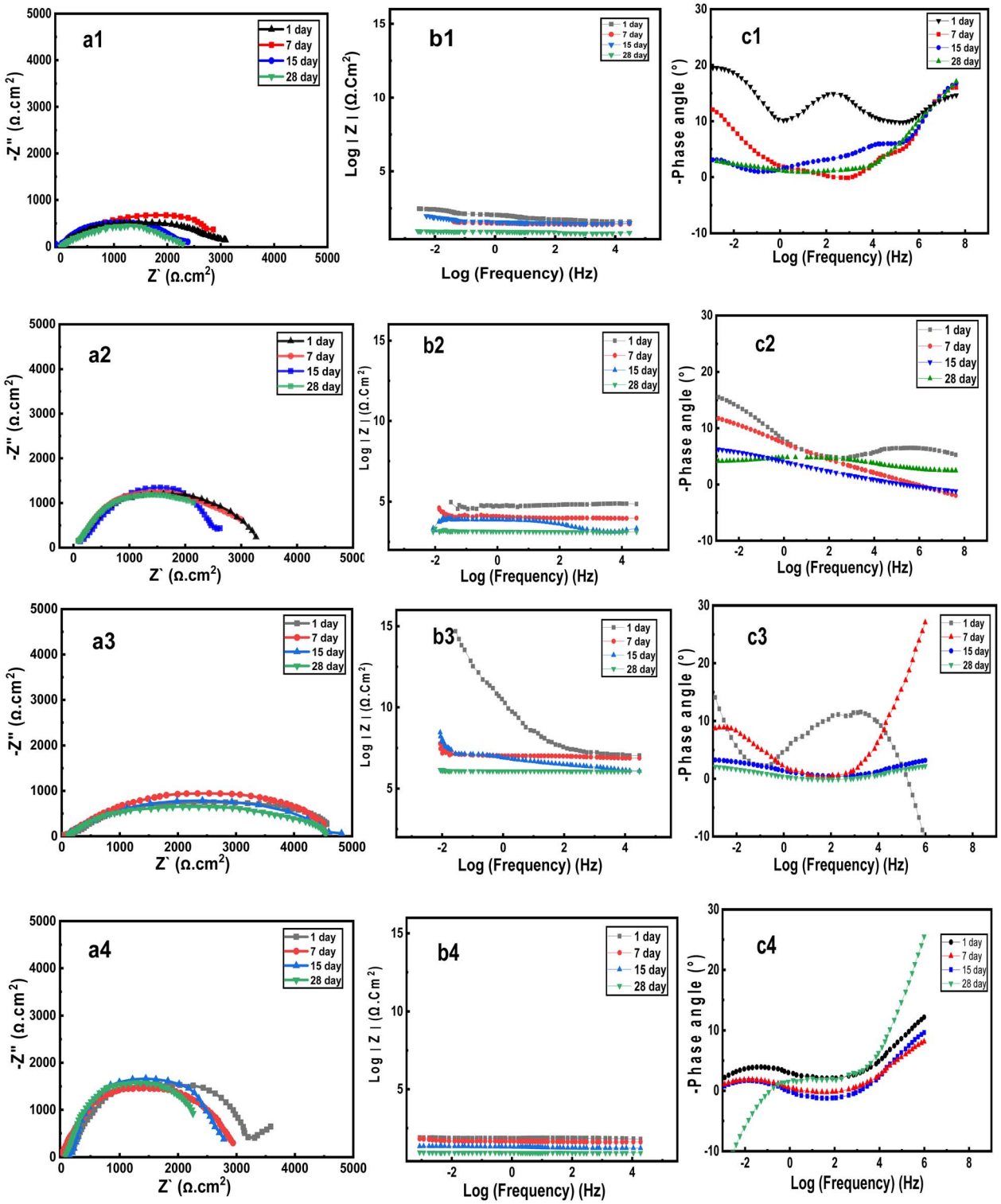


Fig. 6 Electrochemical impedance spectroscopy (EIS) data for mild steel surfaces coated with EMZ1, EMZ2, EMZ3, and EMZ4 in 3.5% NaCl solution over immersion periods of 1, 7, 15, and 28 days. (a) Nyquist plots ($-Z''$ *vs.* $Z'$), (b) Bode modulus plots (log|$Z$| *vs.* log frequency), (c) Bode phase angle plots (−phase angle *vs.* log frequency).

illustrates the distribution of coating thickness across the samples, with EMZ4 exhibiting the highest thickness of 130–200 μm, yet characterized by uneven material accumulation that leads to weak spots and reduced effectiveness. EMZ3 follows with an optimal thickness of 80–120 μm, suggesting a cohesive and stable structure that enhances its protective quality, while EMZ2 and EMZ1 show moderate thicknesses of 100–125 μm and 50–80 μm, respectively, indicating a relatively uniform yet

Table 2 Summary of electrochemical impedance spectroscopy (EIS) parameters for EMZ1, EMZ2, EMZ3, and EMZ4 coatings at selected immersion times in 3.5% NaCl solution

| Sample | Immersion time (days) | $R_{sol}$ (Ω) | $R_p$ (Ω) | $R_{ct}$ (Ω) | $CPE_c$ (F) | $CPE_{dl}$ (F) | $L$ (H) |
|---|---|---|---|---|---|---|---|
| Uncoated mild steel | 28 | 44.7 | — | 2989.16 | — | Present | — |
| EMZ1 | 28 | 44.7 | Present | 2040.85 | Increased (due to ion accumulation) | Increased | — |
| EMZ2 | 28 | 44.7 | Present and increased | 2217.26 | Present | Present | Present (due to degradation) |
| EMZ3 | 28 | 44.7 | Present and increased | 4528 | Present | Decreased | — |
| EMZ4 | 28 | 44.7 | Present | 2067.33 | Present | Increased | Present (due to uneven distribution) |

less optimal distribution that reflects varying degrees of structural integrity.

To further confirm the elemental composition of the coatings and the extent of their alteration post-immersion, EDX was performed, as illustrated in Fig. 5. The results (Fig. 5a and e) for the pristine coating revealed the presence of primary elements C and O, characteristic of the polymer's structural composition. A reduction in the weight percentage of carbon and oxygen was observed after immersion, attributed to the degradation of certain polymer layers and the leaching of polymer components, alongside the emergence of sodium and chlorine from the solution.[56] Fig. 5b and f for the sample EMZ2, characterized by increased zinc oxide content, show a proportional weight percentage of zinc as determined by EDS analysis. Post-immersion, variations in the weight percentages of zinc were observed in samples EMZ1 and EMZ4. Additionally, the absence of sodium ions was noted in the EMZ2 sample, while sample EMZ3 displayed a consistent presence of all detected elements. In contrast, sample EMZ3 exhibited all elements with likely lower degradation, suggesting improved homogeneity and more complex, obstructed pathways.

### 3.4. Electrochemical impedance measurements

To evaluate the performance and quality of the studied coatings in resisting corrosion, electrochemical impedance spectroscopy (EIS) measurements were conducted at various immersion intervals (1, 7, 15, and 28 days) in a 3.5% sodium chloride solution, as depicted in Fig. 6. The key EIS parameters, extracted from the fitting of experimental data to the equivalent circuits, are summarized in the following Table 2 for easy comparison across samples and immersion periods.

For the mild steel sample coated with pure EVA (EMZ1), the Nyquist plot in Fig. 6a1 revealed variations in the diameter of the capacitive loop over different immersion periods. The capacitive loop diameter decreased significantly, achieving an $R_{ct}$ value of 2040.85 Ω after immersion for 28 days compared to its initial value of 2989.16 Ω at the start of immersion, while the solution resistance ($R_{sol}$) remained relatively stable at 44.7 Ω for all samples throughout the immersion periods. This reduction in $R_{ct}$ and the increased capacitance align with SEM images (Fig. 4a, d, e and h) revealing cracks and irregular aggregates, indicating micropore formation and agglomeration as pathways for corrosive species. This was further supported by the Bode plots in Fig. 6b1 and c1, which demonstrated, over a wide range of frequencies, particularly at low frequencies close to 0.01 Hz, a decrease in impedance values with increasing immersion time and a phase angle approaching zero after 28 days. This indicates a breakdown in the coating through the degradation of certain polymer layers, creating pathways and sites susceptible to attack by corrosive species, such as chloride ions or water molecules, thereby reducing the coating's long-term corrosion resistance.

By comparing the EIS results of the EMZ2, EMZ3, and EMZ4 coatings with the above findings, it can be inferred that the incorporation of nano-ZnO into the polymer matrix enhanced the polymer's performance and barrier properties, reducing the penetration of corrosive media and improving the polymer's resistance to long-term degradation, as illustrated in Fig. 6a2–a4. The capacitive loop diameters increased, accompanied by an increase in $R_{ct}$ values, recorded as 2217.26 Ω for EMZ2, 4528 Ω for EMZ3, and 2067.33 Ω for EMZ4 after 28 days of immersion. The moderate $R_{ct}$ (2217.26 Ω) and presence of inductive reactance in EMZ2 correlate with SEM evidence of zinc oxide degradation products (Fig. 5b and f), suggesting agglomeration linked to sacrificial protection. Additionally, impedance and phase angle values increased, as shown in Fig. 6b2–b4 and c2–c4, with variations depending on the ZnO content. A notable increase in capacitance was observed for EMZ1 and EMZ4 due to charge and ion accumulation resulting from the penetration of corrosive species into the coating, promoting polarization within the polymer matrix. In contrast, the EMZ3 sample exhibited high impedance values, indicating the superior efficiency of this coating. The high $R_{ct}$ (4528 Ω) and stable impedance in EMZ3 correspond to SEM images (Fig. 4c and g) showing surface homogeneity and uniform ZnO distribution, reflecting minimal micropore formation. This enhanced protection is attributed to the barrier mechanism, which complicates pathways within the polymer matrix through the formation of hydrogen bonds between the COOH groups of the polymer and the OH groups of zinc hydroxide formed from ZnO

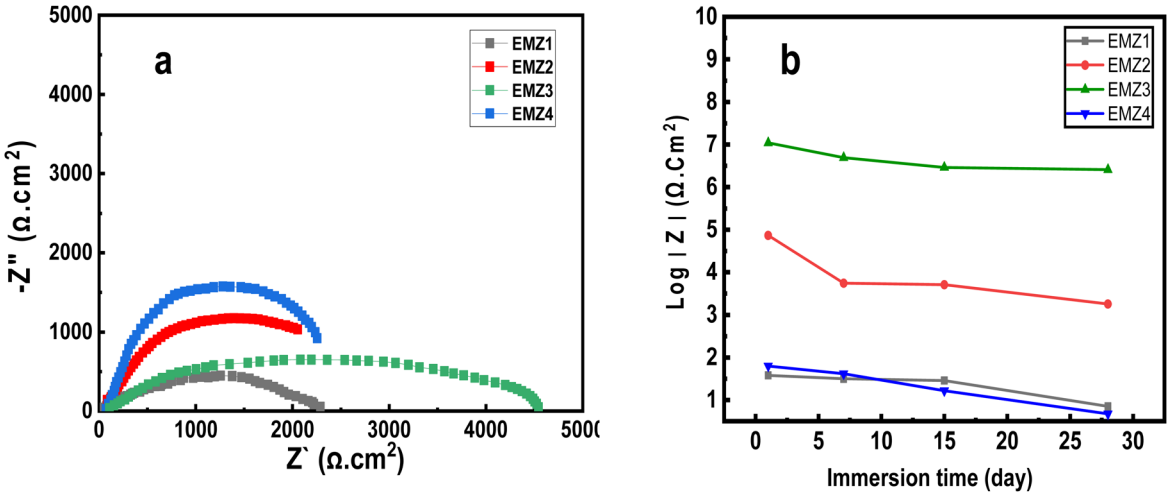


Fig. 7 (a) EIS data of steel covered by various coatings EMZ1, EMZ2, EMZ3, and EMZ4 coatings after 28 days, and (b) the variation of $|Z|$ for different coatings during the immersion in 3.5 wt% NaCl solution for (1, 7, 15, 28) intervals days.

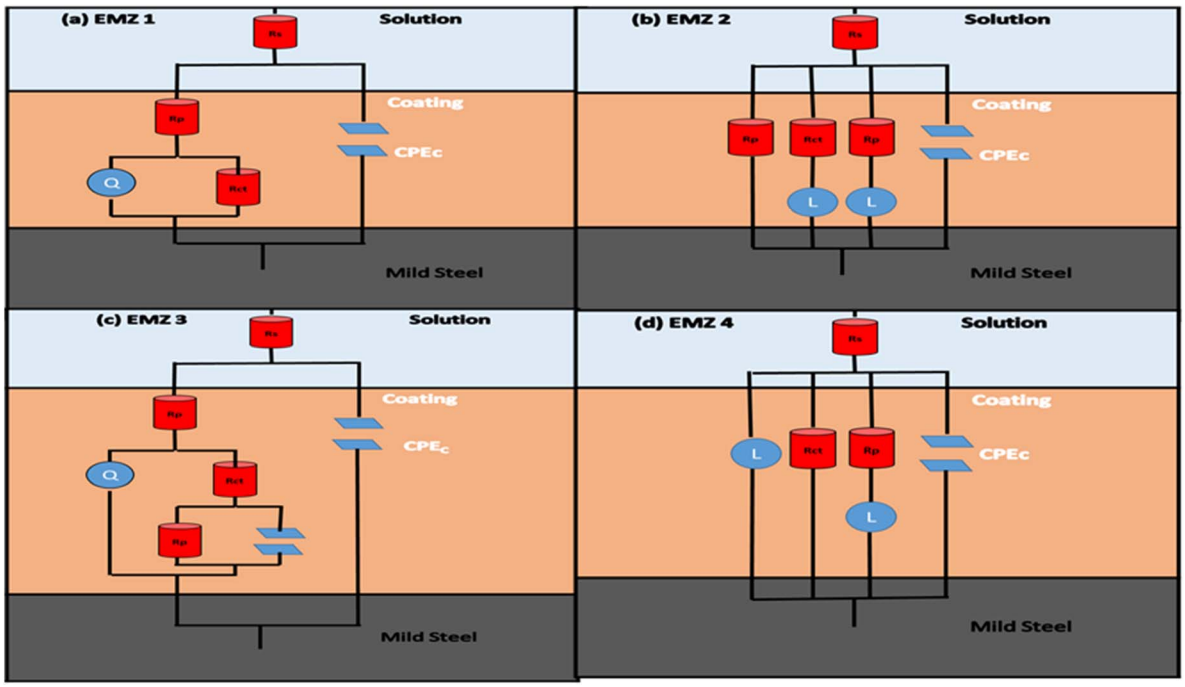


Fig. 8 Equivalent circuit models employed to fit the experimental impedance data for: (a) EMZ1, (b) EMZ2, (c) EMZ3, (d) EMZ4-coated samples.

degradation, as evidenced by XPS results.[57,58] The sacrificial behavior of zinc ions, along with the agglomeration of zinc hydroxide and zinc chloride in potential pores within the polymer layers, provided additional protection.[59] Furthermore, the relatively stable impedance across a wide frequency range, as shown in Fig. 6b3, is attributed to the inferred uniform distribution of ZnO within the polymer matrix, based on the observed homogeneity and performance trends. Conversely, the EMZ4 sample exhibited a pronounced capacitive effect, as depicted in the Nyquist plot (a4), with a significant decrease in $R_{ct}$ (65.21%) and phase angle values approaching zero at low frequencies, potentially due to uneven ZnO distribution, as shown in Fig. 6b4 and c4. This behavior is consistent with SEM-detected aggregates (Fig. 4h), indicating safe pathways for corrosive species within the polymer matrix, leading to a marked reduction in $R_{ct}$ and $R_p$ values, approaching those of EMZ1. This resulted in safe pathways for corrosive species within the polymer matrix, leading to a marked reduction in $R_{ct}$ and $R_p$ values, approaching those of EMZ1. The inductive loop observed in EMZ4, as modeled in the equivalent circuit, is supported by literature on zinc-rich coatings,[60–62] where such loops arise from the relaxation of corrosion products or

adsorption processes at low frequencies. Meanwhile, the observed impedance results are further supported by the thickness profile, where the optimal thickness of 80–120 μm for EMZ3 correlates with its superior resistance of 4528 Ω, while the excessive thickness of 150–200 μm for EMZ4 contributes to its lower protective efficiency with a resistance of 2067.33 Ω.

Fig. 7a illustrates the variation in the performance of the four coatings on mild steel after 28 days of immersion in a 3.5% sodium chloride solution. The EMZ3 sample exhibited the best protective performance compared to EMZ1, EMZ2, and EMZ4. This finding aligns with the previously analyzed electrochemical polarization results, where Fig. 7b demonstrates relatively stable impedance values for EMZ3 across different immersion periods in the 3.5% sodium chloride solution, while EMZ1 and EMZ4 showed deterioration and limited long-term protective capabilities.

In a related context, Fig. 8 provides a representation of the equivalent electrical circuits corresponding to the measured experimental impedance values, as referenced in standard EIS models for nanoparticle-reinforced coatings.[62–64] These circuits include $R_{sol}$ (solution resistance), $R_{ct}$ (charge transfer resistance, reflecting ion or charge transfer resistance), $R_p$ (pore resistance of the coating), $CPE_c$ (coating capacitance), and $CPE_{dl}$ (double-layer capacitance). The models were fitted using ZSimpWin software, which provided automated optimization with acceptable convergence criteria and visual consistency between fitted curves and experimental data (Nyquist and Bode plots in Fig. 6), Additionally, the constant phase element describes deviations from ideal system behavior due to dispersion and distribution. While the inductive reactance ($L$) in EMZ2 and EMZ4 is attributed to phase lags from the formation of intermediates, such as zinc hydroxide, during ZnO degradation.[65]

Finally, the inductive reactance ($L$) may be attributed to phase lag resulting from the formation of intermediates or compounds through adsorption, absorption, precipitation, or expulsion, leading to a time delay in the electrochemical response. This is often a negative indicator of coating weakness and clear evidence of chloride ion penetration, potentially linked to the dynamic relaxation of corrosion products attempting to reach equilibrium after disturbance, particularly at low frequencies, as observed in EMZ2 and EMZ4. However, EMZ2 exhibited good resistance, and the presence of inductive reactance may be attributed to ZnO degradation reactions, promoting positive inductive behavior due to oxidation and reduction processes, known as sacrificial protection, as clearly observed in SEM images.[66] In contrast, the equivalent circuit for EMZ3 reflected a balance between charge transfer resistance and charge retention, with no inductive reactance, supporting the previous findings. The constant phase element in EMZ3 highlighted the coating's electrostatic properties, with $CPE_c$ and $CPE_{dl}$ appearing exclusively in this coating, indicating polarization between degradation products, ZnO, and the polymer's base structure, thereby reinforcing the metal's protective network.[67,68] We note that while the current fit is deemed adequate based on visual alignment, future studies should incorporate detailed statistical validation (*e.g.*, $\chi^2$ and parameter errors) to further substantiate the model's accuracy.

### 3.5. X-ray photoelectron spectroscopy

The XPS analysis, conducted to investigate the chemical states of the EMZ3 coating post-immersion, provides insights into the anticorrosive performance following the corrosion studies. The EIS observation of EMZ3's superior protection, with an $R_{ct}$ of 4528 Ω (Fig. 6a3), is substantiated by XPS data, which confirm the presence of zinc hydroxide and hydrogen bonding with polymer COOH groups, supporting the inferred uniform ZnO distribution within the matrix, as indicated by the stable impedance and SEM homogeneity (Fig. 4c and g).

This validates the barrier mechanism observed in SEM (Fig. 4c and g) and the stable impedance in Fig. 6b3, highlighting EMZ3's chemical stability. For EMZ4, the pronounced capacitive effect and inductive loop (Fig. 6a4) are consistent with XPS evidence of uneven ZnO distribution and degradation products. This aligns with SEM-detected aggregates (Fig. 4h) and supports the EIS-indicated reduction in $R_{ct}$ (2067.33 Ω). Fig. 9 presents the XPS analysis of the EMZ3 sample, which represents a coating composed of ethylene-vinyl acetate (EVA) polymer blended with 60% zinc oxide (ZnO), and applied to mild steel to protect it from corrosion in a 3.5% sodium chloride solution. The coating exhibited superior corrosion resistance after 1 and 28 days of immersion, enhancing polymer degradation and ZnO interaction efficiency through the formation of compounds that seal pores and obstruct corrosion pathways, as illustrated in Fig. 9a and g. These figures highlight variations in peak intensities, particularly for (O, Na, Cl, and Zn).

XPS data confirmed that after 1 day of immersion, the coating maintained its integrity. This is evidenced in Fig. 9b, where the C 1s peak at (285 eV) corresponds to the main hydrocarbon chains of EVA (C–H, C–C), and the peak at (286 eV) represents the acetate group, reflecting the polymer's structural stability. For oxygen (O 1s), as shown in Fig. 9c, a broad peak at (532.5) eV indicates organic oxygen (C–O, O–C=O), with a secondary peak at (530 eV) corresponding to Zn–O, confirming ZnO as a primary component. The Zn 2p spectrum in Fig. 9d displays a Zn ($2p_{3/2}$) peak at (1020.5 eV), with a possible peak at (1034 eV) likely attributed to the Zn LMM Auger signal rather than Zn ($2p_{1/2}$), which typically appears at 1044 eV, based on the standard spin–orbit splitting of approximately (23 eV) for Zn ($2p_{3/2}$) and Zn ($2p_{1/2}$). Sodium chloride deposition is evidenced in Fig. 9e and f, with Na (1s) peaks at binding energies of (1073.4, 1073, and 1074 eV), and Cl (2p) peaks at (198, 200, and 200.5 eV), indicating the presence of chlorine bonded to zinc, sodium, and organic chlorine.

After 28 days of immersion, chemical and physical changes enhanced the coating's protective efficiency. The disappearance of the (286 eV) peak in Fig. 9h suggests degradation of the acetate group in EVA, while an increased intensity at (289 eV) reflects heightened surface oxidation. For oxygen (O 1s), as shown in Fig. 9i, a shift to a primary peak at (531.7 eV), accompanied by secondary peaks at (531.4 and 532.4 eV), indicates the formation of $Zn(OH)_2$. Similarly, the shift of the Zn ($2p_{3/2}$) peak to (1021.5 eV) supports the transformation of ZnO to $Zn(OH)_2$, reinforcing the interpretation that additional

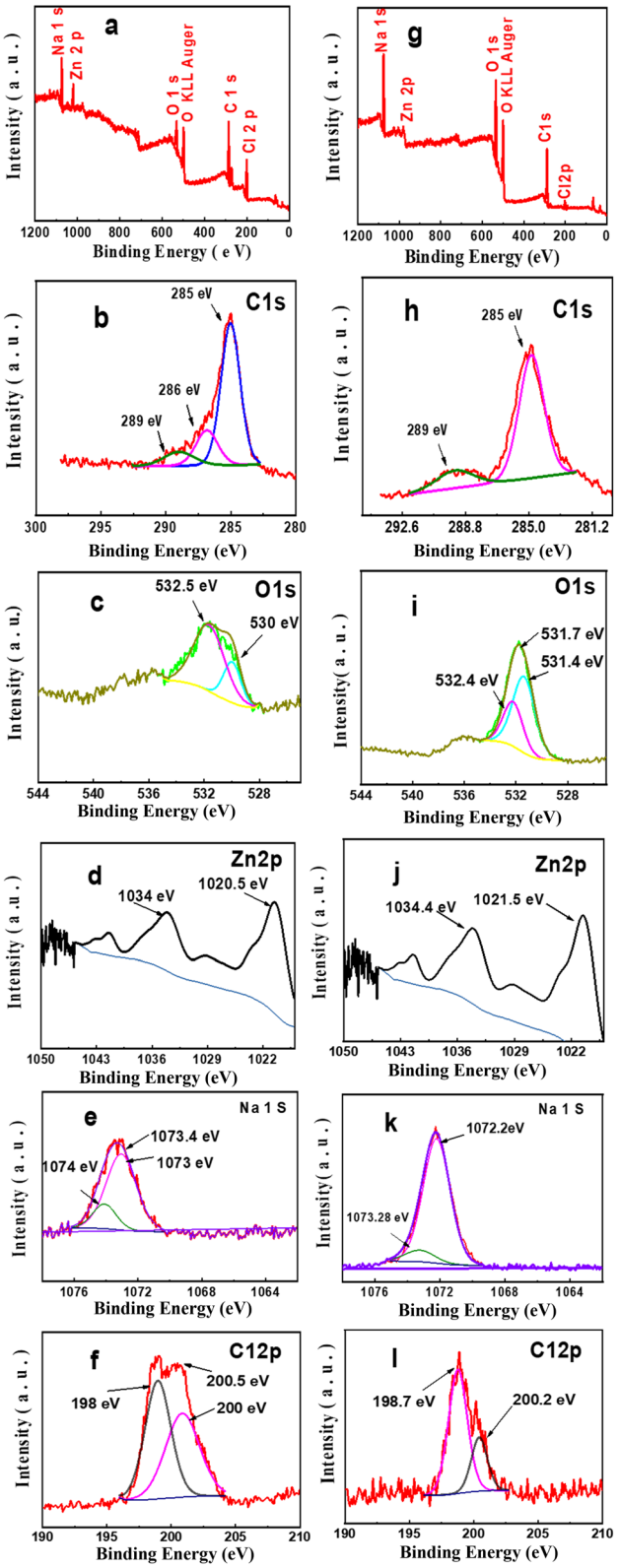


Fig. 9 XPS characterizations of EMZ3; (a–f) coatings after 1 day and (g–l) after 28 days of immersion in 3.5% NaCl.

protective compounds are formed through a sacrificial zinc mechanism that seals pores and blocks pathways for corrosion attack on mild steel.[69] Finally, Fig. 9k and l for Na (1s) and Cl (2p), respectively, show a slight shift with a peak at (1072.2) eV, indicating NaCl deposition, and a minor peak at (1073.2) eV, suggesting the formation of NaOH or $Na_2CO_3$. For Cl (2p), a peak at (198.7 eV) likely corresponds to NaCl, while another at (200.1 eV) indicates $ZnCl_2$ formation, confirming their accumulation and formation.[70]

## 4. Conclusion

In this study, a composite coating comprising ethylene-vinyl acetate (EVA) copolymer and nano-sized zinc oxide (ZnO) at varying concentrations was developed through the mechanical blending method. The results of X-ray diffraction (XRD) and Fourier-transform infrared spectroscopy (FTIR) analyses confirmed the successful integration and interaction between the components, as evidenced by observed shifts in spectral peaks and bands resulting from the interactions between nano-ZnO particles and the macromolecular structure of the polymer matrix. Furthermore, scanning electron microscopy (SEM) images and energy-dispersive X-ray spectroscopy (EDS) results validated the uniform distribution and dispersion of ZnO within the optimal coating, designated as EMZ3, while X-ray photoelectron spectroscopy (XPS) analysis provided insights into the corrosion inhibition mechanism, highlighting the formation of complex pathways facilitated by hydrogen bonding between zinc hydroxide-derived from ZnO degradation- and zinc chloride, which act as sacrificial defense lines to enhance the polymer's primary barrier mechanism. Electrochemical measurements, including electrochemical impedance spectroscopy (EIS), further corroborated the protective properties, with the EMZ3 coating demonstrating superior performance, which polarization resistance surged to 29 219.8 Ω $cm^2$, more than twentyfold higher than the uncoated sample, and a charge transfer resistance of 4528 Ω $cm^2$ that doubled the pure EVA coating's value after 28 days, with impedance stability increasing nearly threefold compared to EMZ4. Notably, elevating the ZnO content from 60% in EMZ3 to 80% in EMZ2 improved protection efficiency by an additional 0.5%, though excessive agglomeration reduced efficacy by 0.2% due to disrupted matrix integrity, underscoring the critical role of uniform dispersion; these groundbreaking findings, attributed to the optimal ZnO distribution without agglomeration. This study is expected to inspire researchers to explore sustainable strategies by evaluating and developing novel composites based on EVA polymers and other nano-oxides, while also opening avenues for incorporating recycled polymers from industrial waste to produce more efficient, environmentally friendly, cost-effective, and simpler-to-manufacture protective coatings.

## Conflicts of interest

There are no conflicts to declare.

## Data availability

All data is available within the manuscript.

## References


1 H.-D. Yu, Z. Zhang and M.-Y. Han, *Small*, 2012, **8**(17), 2621–2635.
2 B. C. Bunker and W. H. Casey, *Oxide Films in Metal Corrosion: Oxide Defect Chemistry*, Oxford University Press, 2016.
3 J. Wang, H. Yu, H. Du, M. Wan, J. Wang, S. Chang, P. Zhang, P. Shi, D. Sun and Y. Wang, *Appl. Sci.*, 2024, **14**(24), 11565.
4 Y. Li, X. Zhao, Y. Guan, H. Li and X. Zhang, *Front. Phys.*, 2023, **11**, 1277710.
5 D. Xu, T. Gu and D. R. Lovley, *Nat. Rev. Microbiol.*, 2023, **21**(11), 705–718.
6 D. K. Park, D. H. Park, H. B. Kim, B. J. Kim, J. K. Seo and J. K. Paik, *Struct. Eng. Mech.*, 2012, **42**(4), 531–549.
7 F. Sun, X. Li, F. Zhang, X. Cheng, C. Zhou, N. Wu, Y. Yin and J. Zhao, *Acta Metall. Sin. (Engl. Lett.)*, 2013, **26**(3), 257–264.
8 Q. Li, X. Wang, Z. Pei, K. Xiao, X. Yang and X. Cheng, *Materials*, 2025, **18**(10), 2299.
9 X. Xu, L. Tian, Y. Zhou, M. Sun, X. Wang, C. Shang and R. D. K. Misra, *J. Iron Steel Res. Int.*, 2019, **26**(6), 611–620.
10 D. Ok, *J. Ship Prod. Des.*, 2019, **35**(04), 299–308.
11 S. K. Sharma and A. Sharma, *Green Corrosion Inhibitors: Status in Developing Countries*, 2011, pp. 157–180.
12 D. T. Oyekunle, A. O. Ayeni and O. Agboola, *J. Phys.: Conf. Ser.*, 2019, **1378**(3), 032046.
13 P. Shetty, *S. Afr. J. Chem.*, 2018, **71**(1), 46–50.
14 S. Subash and S. Moharana, *Electrochemical Society Meeting Abstracts MA2023-02(11)*, 2023, p. 1078.
15 W. Fürbeth, *Materials*, 2020, **13**(15), 3401.
16 H. Vasudev and L. Thakur, *J. Electrochem. Sci. Eng.*, 2024, **14**(4), 417–418.
17 A. Maury-Ramírez, H. Kanematsu and I. Flores-Colen, *Coatings*, 2020, **10**(8), 728.
18 D. Bian and Y. Zhao, *Russ. J. Appl. Chem.*, 2015, **88**(10), 1718–1722.
19 D. Bian, Y. Zhao and Y. Guo, *Russ. J. Appl. Chem.*, 2016, **89**(12), 2091–2094.
20 V. C. C. Checchin, A. Gonzalez, M. Bertuola and M. A. F. L. de Mele, *Prog. Org. Coat.*, 2022, **172**, 107068.
21 A. Horcher, K. Tangermann-Gerk, W. Krenkel, M. Schmidt, S. Schafföner and G. Motz, *J. Eur. Ceram. Soc.*, 2024, **44**(11), 6607–6619.
22 O. V. Savvova, *Glass Ceram.*, 2014, **71**, 254–257.
23 A. V. Ryabova, E. A. Yatsenko, L. V. Klimova, E. V. Filatova and A. Y. Velichko, *Glass Phys. Chem.*, 2017, **43**(1), 34–42.
24 R. Hosseini Rad, M. Toorani and H. R. Zarei, *Anti-Corros. Methods Mater.*, 2018, **66**(1), 138–147.
25 S. J. Skosana, C. Khoathane and T. Malwela, *Polym. Bull.*, 2020, **78**(1), 203–221.
26 B. Xu, K. Z. Miao, B. Y. Lou and J. Yang, *Adv. Mater. Res.*, 2010, **152**, 1262–1266.
27 A. Kaviarasi, M. L. V. Kumari and A. Anandhavadivel, *Int. J. Chem. Sci.*, 2018, **16**(4), 296.
28 M. Sobhy, A. I. Eid, A. Saleh and W. M. Khairaldien, *IOP Conf. Ser.: Mater. Sci. Eng.*, 2020, **975**(1), 012003.
29 B. Afrinaldi, D. N. Vicarneltor, R. P. Rudianto, A. R. Hakim and O. F. Muslim, *Mater. Sci. Forum*, 2021, **1028**, 234–239.
30 H. S. Majeed, F. K. H. Al-Juboory, R. Hamid and R. M. Zawawi, *Polimery*, 2023, **68**(3), 135–141.
31 A. Ndukwe, J. Anumudu, C. Ugwuegbu, C. Onuoha, P. Nnajih, A. Aleme, P. Anozie, C. Augustine, D. Benson, O. Charles-Oluka and C. Okonkwo, *Acta Period. Technol.*, 2025, 12.
32 X. Yu, L. Wang, L. Liu, Y. Wang, Z. Zhang and P. Yang, *J. Appl. Polym. Sci.*, 2018, **135**(27), 46421.
33 M. A. Y. Barakat and A. E.-A. A. El-Wakil, *Mater. Res. Express*, 2021, **8**(10), 105304.
34 B. X. Du, J. Li and Y. Sekii, *IEEE Trans. Dielectr. Electr. Insul.*, 2017, **24**(3), 1503–1510.
35 A. G. Al-Gamal, W. S. Gado, M. A. Abo El-Khair, K. Zakaria, A. A. Ragab and K. I. Kabel, *Sci. Rep.*, 2024, **14**(1), 28352.
36 M. Gervasio and K. Lu, *J. Phys. Chem. C*, 2017, **121**(21), 11862–11871.
37 V. Gilja, I. Živković, T. Klaser, Ž. Skoko, M. Kraljić Roković, Z. Hrnjak-Murgić and M. Žic, *Catalysts*, 2020, **10**(4), 400.
38 M. Naskar, H. M. Dharmendra and G. L. Sarode, *Mater. Today: Proc.*, 2020, **27**, 1939–1942.
39 J. Liu and S. S. Jia, *Adv. Mater. Res.*, 2011, **183–185**, 1864–1868.
40 M. K. Lila, *NeuroQuantology*, 2022, **20**(8), 10430–10439.
41 F. Fekri, M. M. Foroughi and M. Shahidi Zandi, *Iran. Polym. J.*, 2019, **28**(7), 577–585.
42 S. Kasisomayajula, V. Johnston Gelling and N. Jadhav, Recent Advances in Polymer Nanocomposite Coatings for Corrosion Protection, *Advances in Nanostructured Composites*, 2019, pp. 241–277.
43 P. Selvakumar, H. S. Punna, M. K. Gupta, S. K. Nathsharma and K. Singh, *Corrosion Protection*, IGI Global, 2025, pp. 167–186.
44 V. Dalmoro, J. H. Z. Dos Santos and C. Santos, *Smart Coatings for Corrosion Protection*, Springer, 2016, pp. 417–435.
45 J. Sebastian, E. T. Thachil, J. J. Mathen, J. Madhavan, P. A. Thomas, J. Philip, M. S. Jayalakshmy, S. Mahmud and G. P. Joseph, *Open J. Compos. Mater.*, 2015, **5**(3), 79–91.
46 S. Moussa, F. Namouchi and H. Guermazi, *Eur. Phys. J. Plus*, 2015, **130**(7), 152.
47 A. Mohammadi and S. Pourmoslemi, *Water Sci. Technol.*, 2018, **2017**(3), 791–801.
48 B. Xu, W. Ma, X. Bi, L. Shao and L. Qian, *J. Polym. Environ.*, 2019, **27**(5), 1127–1140.
49 J. A. Jofre-Reche and J. M. Martín-Martínez, *Int. J. Adhes. Adhes.*, 2013, **43**, 42–53.
50 A. Sachdeva, S. Singh and P. K. Singh, *Mater. Today: Proc.*, 2021, **34**, 697–701.
51 S. M. Mirabedini and K. Khodabakhshi, Nanocomposites of PU polymers filled with spherical fillers, in *Polyurethane Polymers*, Elsevier, 2017, pp. 135–172.
52 S. Ez-Zahraoui, A. E. K. Qaiss, R. Bouhfid, M. ElAchaby and F. Z. Semlali, *J. Thermoplast. Compos. Mater.*, 2025, DOI: 10.1177/08927057251344146.
53 M. Chennimalai, V. Vijayalakshmi, T. S. Senthil and N. Sivakumar, *Mater. Today: Proc.*, 2021, **47**, 1842–1846.

54 B. Xu, W. Ma, L. Shao, L. Qian and Y. Qiu, *R. Soc. Open Sci.*, 2019, **6**(3), 181413.
55 D. V. Hiscott, Light downshifting zinc oxide-ethylene vinyl acetate nanocomposite greenhouse films, Doctoral dissertation, The University of Western Ontario, Canada, 2020.
56 G. K. Bhagavatula, S. Leena, K. Murugasamy, R. Nanoth, S. Narayanan, A. Pegoretti and J. Karingamanna, *Surf. Interfaces*, 2024, **55**, 105477.
57 M. Mobin, J. Aslam and R. Alam, *Arabian J. Sci. Eng.*, 2017, **42**(1), 209–224.
58 A. Rajendran, T. Sivalingam, P. Narayanan and S. C. Murugavel, *Am. J. Appl. Chem.*, 2018, **6**(3), 102.
59 A. Kherfi, A. Madani, D. Chalal and S. Benidir, *Synth. Met.*, 2021, **277**, 116795.
60 B. Li, D. Li, W. Xia and W. Zhang, *Appl. Surf. Sci.*, 2018, **458**, 665–677.
61 S. Ghaziof, P. A. Kilmartin and W. Gao, *J. Electroanal. Chem.*, 2015, **755**, 63–70.
62 M. J. A. Santos, W. O. Júnior, J. K. L. Ribeiro, N. C. Maciel, I. N. Bastos, J. N. Pereira, P. N. da Costa Souza, H. C. Pinto and E. P. da Silva, *J. Alloys Compd.*, 2024, **1002**, 175339.
63 R. Ding, S. Chen, N. Zhou, Y. Zheng, B. Li, T. Gui, X. Wang, W. Li, H. Yu and H. Tian, *J. Alloys Compd.*, 2019, **784**, 756–768.
64 F. Deng, L. Wang, Y. Zhou, X. Gong, X. Zhao, T. Hu and C. Wu, *RSC Adv.*, 2017, **7**(77), 48876–48893.
65 J. W. Soedarsono, A. Andoko, K. Diharjo, F. Gapsari, S. M. Rangappa and S. Siengchin, *Case Stud. Chem. Environ. Eng.*, 2025, **11**, 101039.
66 J. Liu, F. Wang and K. C. Park, *Mater. Corros.*, 2011, **62**(11), 1008–1014.
67 D. M. Xie, T. Y. Wang, J. P. Xie, F. Y. Cao and Y. G. Wang, *Corros. Eng., Sci. Technol.*, 2023, **58**(8), 734–746.
68 Sh. Ammar, K. Ramesh, B. Vengadaesvaran, S. Ramesh and A. K. Arof, *Prog. Org. Coat.*, 2016, **92**, 54–65.
69 S. Wang, R. Yue, Y. Pan, X. Meng, R. Zhu, Y. Zuo, D. Zeng and S. Sheng, *Mater. Today Commun.*, 2025, **47**, 113070.
70 K. A. Yasakau, A. Kuznetsova, H. M. Maltanava, S. K. Poznyak, M. G. S. Ferreira and M. L. Zheludkevich, *Corros. Sci.*, 2024, **229**, 111889.